Magnetic Dipole and Electric Quadrupole Hyperfine Effects in Bi^{209} Muonic X Rays*

T. T. BARDIN,† R. C. COHEN, S. DEVONS, D. HITLIN, E. MACAGNO, J. RAINWATER, K. RUNGE,‡ AND C. S. WU
Columbia University, New York, New York

AND

R. C. BARRETT
Columbia University, New York, New York and Lawrence Radiation Laboratory, University of California, Berkeley, California

(Received 6 March 1967)

The muonic x rays from the spherical nucleus Bi^{209} were detected by Li-drifted germanium detectors with an energy resolution of 0.14% at 6-MeV γ energy. The following information was obtained: (1) The hfs due to the $M1$ and $E2$ interactions between the muon and the nuclear charge and magnetic moment distributions was observed. The theoretically predicted splittings based on different nuclear models were compared with the experimental results. (2) The parameters of the spherical charge distribution as described by the "Fermi distribution" were determined from the transition energies of the K and L muonic x rays: $c=(1.126_{-0.006}{}^{+0.008})A^{1/3}$ fm and $t=4\log_e 3\,(0.511_{-0.033}{}^{+0.026})$ fm. (3) The experimental results confirm the anomalous intensity ratios previously observed in Bi muonic x rays. The observed intensity ratios were $(2p_{3/2}\rightarrow 1s_{1/2}):(2p_{1/2}\rightarrow 1s_{1/2})=1.38\pm0.1$, $(3d_{5/2}\rightarrow 2p_{3/2}):(3d_{3/2}\rightarrow 2p_{1/2})=1.5\pm0.1$, and $(4f_{7/2+5/2}\rightarrow 3d_{5/2}):(4f_{5/2}\rightarrow 3d_{3/2})=1.29\pm0.3$. (4) The cascade transitions in the sequence $4f\rightarrow 3d\rightarrow 2p\rightarrow 1s$ are approximately equal in intensity within an uncertainty of 15%.

I. INTRODUCTION

IT has been shown in the past[1,2] that muonic x rays can be used as a sensitive means to determine the effective charge radius of a finite nucleus. However, if the hyperfine structure (hfs) of the muonic x rays can be observed or resolved, then the distribution of magnetic dipole ($M1$) and electric quadrupole ($E2$) moments in the nucleus can be investigated as well. The $M1$ and $E2$ moments have long been studied through the hfs of optical spectra. However, there are several important advantages in using muonic x rays over the optical spectra in investigating these effects. Firstly, the Bohr radius of the muonic atom is about 207 times smaller than that of the electronic atom; therefore, the muon wave function in a $1s$ or $2p$ state is not affected by the screening effect of the remaining electrons and can be calculated exactly if the charge distribution is known. Secondly, the ratio for the $M1$ hfs constant a to the binding energy E in the muonic atom is about 207 times larger than that of the ordinary atom. Thirdly, because the muon spends a large fraction of its time inside the nucleus, the muon is much more sensitive to nuclear properties, such as charge or nuclear moment distributions, than the electron.

Bohr and Weisskopf have shown that owing to the distribution of the magnetic dipole moment inside a finite nucleus, the hfs effect is, in general, smaller than that to be expected for a point nucleus. This effect is known as the Bohr-Weisskopf[3] (BW) effect, and should be observable in muonic atoms. Furthermore, since various types of nuclear models predict different distributions of the nuclear dipole moment, the experimental measurement of the BW effect should provide a crucial test for the various nuclear models.

Our recent observation and analysis of the hfs of $M1$ and $E2$ interactions in the Bi^{209} nucleus has been briefly reported.[4] Similar experiments in Bi^{209} have also been briefly reported by other laboratories.[5] In this paper, we shall describe and discuss our experimental methods and results in more detail. Furthermore, the results from the analysis of the charge distribution of the Bi^{209} nucleus will be included.

II. THEORY

Regarding the $M1$ and $E2$ interactions in muonic K x rays, we will first show that the ratio for the $M1$ hfs constant a to the binding energy E for the muonic atom is 207 times that of the ordinary atom. The $M1$ hfs constant a for the $1s_{1/2}$ state of a given atomic particle (e.g., electron or muon) can be expressed as

$$a=(16/3)\pi g_I\mu_a\mu_N|\psi_s(0)|^2,$$

where μ_N and μ_a are the magnetic moments of nucleus

* Work partially supported by the U. S. Atomic Energy Commission and the U. S. Office of Naval Research.

† Work done in partial fulfillment of the requirements for the Ph.D. degree. Present address: Haverford College, Haverford, Pennsylvania.

‡ On leave from II. Physikalisches Institut, University of Heidelberg, Heidelberg, Germany.

[1] V. L. Fitch and J. Rainwater, Phys. Rev. **92**, 789 (1953).

[2] W. Frati and J. Rainwater, Phys. Rev. **128**, 2360 (1962).

[3] A. Bohr and V. F. Weisskopf, Phys. Rev. **77**, 94 (1950).

[4] T. T. Bardin, R. C. Barrett, R. C. Cohen, S. Devons, D. Hitlin, E. Macagno, C. Nissim-Sabat, J. Rainwater, K. Runge, and C. S. Wu, Phys. Rev. Letters, **16**, 429 (1966).

[5] R. D. Ehrlich, D. Fryberger, D. A. Jensen, C. Nissim-Sabat, R. J. Powers, B. A. Sherwood, and V. L. Telegdi, Phys. Rev. Letters, **16**, 425 (1966). S. Raboy, R. E. Cote, R. Guso, R. A. Carrigan, Jr., A. Gaigalas, R. B. Sutton, and C. C. Trail, Bull. Am. Phys. Soc., **11**, 129 (1966). H. L. Acker, G. Backenstoss, C. Daum, J. C. Sens, and S. A. DeWit, Nucl. Phys. **87**, 1 (1966).

and the atomic particle, respectively. For a spin-$\frac{1}{2}$ particle, $\mu_a = e\hbar/2m_a c$; where m_a is the mass of the atomic particle. Furthermore, for low-Z nuclei, one may write

$$|\psi_s(0)|^2 \approx \frac{1}{\pi}\left(\frac{m_a e^2 Z}{\hbar}\right)^3.$$

Therefore, the $M1$ hfs constant a is proportional to m_a^2. On the other hand, the binding energy

$$E \cong -\tfrac{1}{2} m_a c^2 \left(\frac{Ze^2}{\hbar c}\right)^2$$

is proportional to m_a so that

$$a(\mu)/E(\mu)/a(e)/E(e) \cong \frac{m_\mu}{m_e} \cong 207.$$

In spite of the relatively larger $M1$ hfs constant in the muonic atom as compared with the ordinary atom, the $M1$ interaction in muonic atoms is, in general, two orders of magnitude smaller in comparison with the $E2$ interaction on account of the 207 times smaller value of the muon magnetic moment μ_a. This is shown by the expression

$$\langle \mu_N \mu_a / r^3 \rangle / \langle e^2 Q / r^3 \rangle .$$

This ratio for atomic electrons is approximately equal to 1. Therefore, the $M1$ hfs can be best studied in the absence of large quadrupole interactions. In particular, it is advantageous to study the hfs of the $2p_{1/2} \rightarrow 1s_{1/2}$ transitions of a spherical nucleus where the effect of the $E2$ interactions vanishes. The Bi^{209} nucleus is very well suited for the investigation of $M1$ interactions as it has only one proton outside the doubly magic core, so it can be considered a spherical nucleus and described reasonably accurately by the shell model. The ground-state spin of Bi^{209} is $\frac{9}{2}$ and its measured magnetic dipole moment is $\simeq 4.08$ nm. The experimentally measured electric quadrupole moment of Bi^{209} is approximately -0.4 b.

Bohr and Weisskopf[5] have calculated the influence of the finite distribution of nuclear magnetization on the hfs of $1s_{1/2}$ and $2p_{1/2}$ electrons. Stroke *et al.*[6] extended the calculation assuming the more complicated configuration-mixing model for the nucleus. Le Bellac[7] generalized the case for arbitrary muonic states $|l,j\rangle$ and assumed various nuclear models in the calculation of nuclear magnetization.

The energy displacement ΔW_F due to the magnetic interaction for the state of total angular momentum $\mathbf{F}(\mathbf{F}=\mathbf{I}+\mathbf{J}$; $\mathbf{I}$ and $\mathbf{J}$ being the total angular momentum for the nucleus and the muon, respectively) is expressed as follows:

$$\Delta W_F = \frac{1}{2IJ}[F(F+1)-I(I+1)-J(J+1)]A_1,$$

where A_1 is equal to IJa (a is the hfs constant).

A_1 represents the magnetic interaction between the nucleus and the muon. A_1, therefore, depends on the distribution of the nuclear magnetic moment, which comprises two intrinsically different parts, a spin moment and an orbital moment. The following nuclear models were employed in the calculation of A_1[7]: the point-nucleus model, the single-particle shell model, and the configuration-mixing model. Harmonic-oscillator wave functions were used to approximate the nuclear wave function. The muon wave functions were those obtained by Ford and Wills.[8]

The calculated values[7] of A_1 are listed in Table I.

Thus the hfs constant is reduced by almost 50% in the configuration-mixing model in comparison with the unrealistic point-nucleus model.

The hyperfine energy displacement of electric quadrupole origin is

$$\Delta W_F = \frac{6[K(K+1)-\frac{4}{3}I(I+1)J(J+1)]A_2}{2I(2I-1)2J(2J-1)},$$

where $K=F(F+1)-I(I+1)-J(J+1)$.

A_2 again depends on the nuclear model assumed. Le Bellac[7] calculated the value A_2 to be -3.02 keV, using the single-particle shell model for simplicity. However, this A_2 value was corrected by a factor which is the ratio of the observed quadrupole moment to the single-particle quadrupole moment: $A_2'' = -3.02 \times 0.4/0.44 = -2.74$ keV. The configuration mixing model was not applied here, since the mixing amplitudes required to fit the observed magnetic dipole moment give a quadrupole moment much larger than the experimental value derived from the atomic-beam magnetic-resonance measurement.[9]

In the $1s_{1/2}$ and the $2p_{1/2}$ states only the magnetic interaction gives rise to the hfs. In the $2p_{3/2}$ state, both the electric quadrupole interaction and the magnetic interaction contribute to the hfs and usually the former dominates the splitting.

Applying the dipole selection rules $\Delta F = 0, \pm 1$, we obtain the transition energies shown in Figs. 1 and 2. The relative intensities of the transitions are derived from purely statistical population of the levels.

III. EXPERIMENTAL ARRANGEMENT AND ANALYSIS

A. Detectors and Electronics

Two lithium-drifted germanium detectors, each with an active volume of ~ 7 cm$^2 \times 9$ mm, fabricated at the

[6] H. H. Stroke, R. J. Blin-Stoyle, and V. Jaccarino, Phys. Rev. **123**, 1326 (1961).
[7] M. Le Bellac, Nucl. Phys. **40**, 645 (1963).
[8] K. Ford and J. Wills, Nucl. Phys. **35**, 295 (1962).
[9] R. S. Title and K. F. Smith, Phil. Mag. **5**, 1281 (1960).

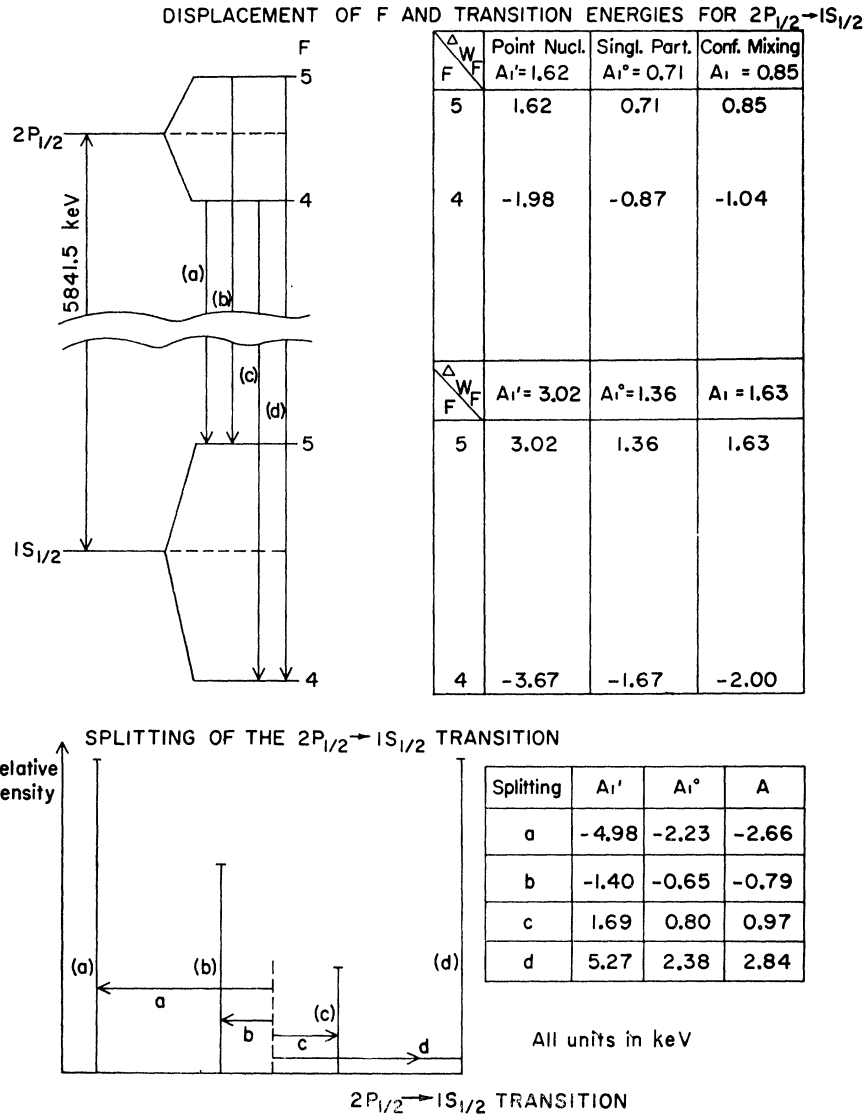

ΔW_F / F	Point Nucl. A_1'= 1.62	Singl. Part. A_1^0= 0.71	Conf. Mixing A_1 = 0.85
5	1.62	0.71	0.85
4	-1.98	-0.87	-1.04
ΔW_F / F	A_1'= 3.02	A_1^0= 1.36	A_1 = 1.63
5	3.02	1.36	1.63
4	-3.67	-1.67	-2.00

Splitting	A_1'	A_1^0	A
a	-4.98	-2.23	-2.66
b	-1.40	-0.65	-0.79
c	1.69	0.80	0.97
d	5.27	2.38	2.84

All units in keV

FIG. 1. The theoretical $M1$ hfs splitting for the $2p_{1/2}$ and the $1s_{1/2}$ levels and for the $2p_{1/2} \rightarrow 1s_{1/2}$ transition, including the Bohr-Weisskopf effect for the single-particle shell model and the configuration-mixing model and the comparison with the point nucleus as given in Ref. 7. The relative intensities of the hfs components are calculated based on the statistical population of the levels.

Pegram Nuclear Physics Laboratory,[10] were used in the experiment. The resolution of the detectors, including the electronic noise, is 3.8 keV for γ rays around 1 MeV and 8.5 keV for γ rays in the 5–6-MeV region. The detectors were housed and operated in a high-vacuum system at liquid-nitrogen temperature and with a bias voltage of $\sim$1000 V. The charge collection time of the Ge(Li) detectors operated under the above conditions is $\sim$25 nsec.

The electronic equipment associated with the detector can be divided into two functions: (1) the conversion of the collected charge from the detector into a voltage pulse which provides information on the energy of the x rays—this is equivalent to the conventional "slow signal" for NaI work, and (2) the generation of a timing signal from the leading edge of the charge collection pulse—the conventional "fast signal" which is to be used in coincidence with the beam telescope output.

The slow signal is obtained from a low-noise fast-rise charge-sensitive preamplifier which converts the collected charge pulses into voltage pulses linearly. The signals from the output of the charge-sensitive pre-

[10] K. Runge and C. S. Wu, NYO-GEN-72-28, pp. 74–77 (1964–65) (PNPL), Columbia University (unpublished).

TABLE I. Values of the hfs constant for the $1s_{1/2}$ and the $2p_{1/2}$ states for the point-nucleus, the single-particle, and the configuration-mixing models as in Ref. 7.

Level	A_1' point nucleus (keV)	A_1^0 single particle (keV)	A_1 configuration-mixing (keV)	$(A_1'-A_1)/A_1'$
$1s_{1/2}$	3.02	1.36	1.63	46%
$2p_{1/2}$	1.62	0.71	0.84	48%

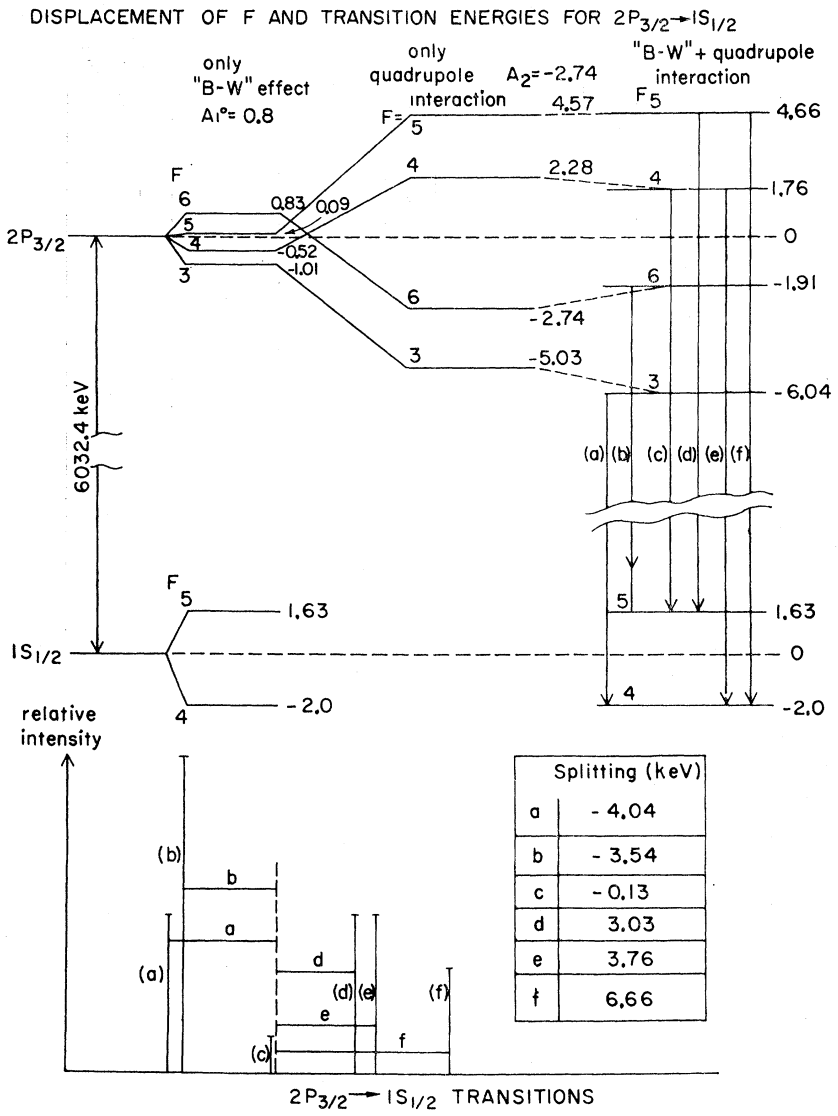

FIG. 2. The theoretical $M1$ and $E2$ hfs splitting of the $2p_{3/2}$ and $1s_{1/2}$ levels and for the $2p_{3/2} \rightarrow 1s_{1/2}$ transition calculated with values of A_1 and A_2 as given in Ref. 7.

amplifier are further amplified by a band-limited, double *RC*-shaped low-noise linear amplifier which offers optimum noise rejection and provides the pulse shape required for the input of the Victoreen SCIPP 1600-channel analyzer. The stability of the complete assembly was tested to be better than one in 1600 channels in 24 h if room temperature did not vary more than $\pm 1°C$, and the integral linearity of the assembly was better than 0.1%. There was no apparent change of spectral line shape between the beam-on and beam-off conditions. However, there was a slight shift of the base line between the beam-on and beam-off conditions; therefore, in the final energy determination of the bismuth muonic x rays, the spectrum was calibrated against the full-energy photopeak and the escape peak of the well-known 2.6145-MeV γ lines[11] from Pb^{208*}, a product of muon capture in Bi^{209}. If a particular region of the spectrum was to be displayed on the multichannel analyzer, a window amplifier was employed.

The fast signal provides a timing pulse, so it should have a minimum of time jitter. A fast rise (<10 nsec) double-delay-line amplifier was used to fulfill this requirement. The zero-crossing time of the double-delay-line amplifier is rather insensitive to the input pulse height; jitter, then, depends only on the noise level and the rise time of the signal. A single-channel analyzer was used to select the zero-crossing time. Its lower bias was adjusted to reduce the noise from the double-delay line and the low-energy background in the x rays; its upper level discriminator was adjusted to eliminate saturation pulses from the double-delay-line amplifier. The timing signal was put into coincidence with the beam telescope and the coincidence pulse served as the gating signal of the multichannel analyzer.

[11] G. Murray, R. L. Graham, and J. S. Geiger, Nucl. Phys. 63, 353 (1965).

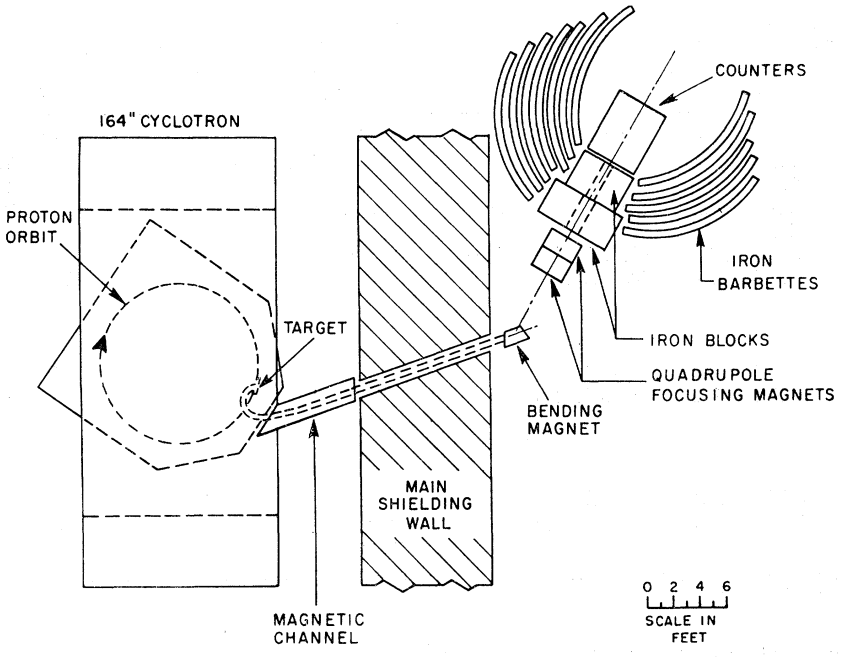

FIG. 3. The floor plan of the cyclotron beam layout.

B. Beam and Beam Telescope

The negative muon beam was extracted from the Columbia University Nevis Synchrocyclotron in a manner very similar to previous muonic x-ray investigations reported from this laboratory. The floor plan is shown in Fig. 3. The momentum-analyzed beam is slowed down by polyethylene slabs, the thickness of which was adjusted to stop most of the pions. The remainder of the beam consists mostly of muons, electrons, and γ rays. The contamination of fast electrons in the beam would cause a large increase in the background counting rate. It was effectively removed by using two velocity-selective Čerenkov counters, one of water and the other of Lucite. The electrons, mostly of the same momentum as the remaining components of the beam, have a higher velocity than the muons, and therefore produce Čerenkov light. These electron pulses can be selected out from the muon pulses and used to produce anticoincidence pulses.

The whole beam telescope assembly consists of four plastic scintillation counters and two Čerenkov counters. The schematic of the counter arrangement is shown in Fig. 4. The Ge(Li) detectors are placed in the muon beam in order to obtain a maximum solid angle. Typical muon stopping rates are 600/sec for a target of $3 g/cm^2$ and 5 in.$\times$5 in. Coincident signals derived from counters 1 and 2, and one or both of the Čerenkov counters denoted as $12C_1$ and/or $12C_2$ represent electron signals. Coincident signals from counters 1, 2, and 3 are put in anticoincidence with counter 4, i.e., $(123\bar{4})$ representing a stopping muon or electron. Since only muons are of interest, the logic $(123\bar{4})$ in anticoincidence with $12C_1$ or $12C_2$, i.e., $(123\bar{4})\sim(12C_1$ or $12C_2)$, where tilde means "not," is used to characterize a muon stop in the target. The complete electronic block diagram is shown in Fig. 5.

The duration of each run varied from 4 to 5 h, depending upon the counting rate. Line shifts due to electronic instability or temperature effects were checked using natural radioactive sources, e.g., Na^{22}, Na^{24}, Cs^{137}, Co^{60}, and the 6.131-MeV γ-rays from the $O^{16}(n,p)N^{16*}(\beta,\nu)O^{16*}$ reaction, and by using a precision pulser before, after, and sometimes during each run.

C. Data Analysis

The complete data analysis was performed with the aid of a PDP4 computer equipped with a Calcomp plotter. Owing to the poor statistics of each individual run, the data shown in all figures are summed experimental results of five runs.

1. Energy Determination

In order to sum all individual runs, each run must be corrected for any relative gain shifts and shifts of the base line occurring during the run. This is done by first locating the centroids of all the prominent peaks appearing on the individual runs. By comparing the centroids of the peaks from these runs with a preselected run, one can determine both the gain shift and the shift of the zero offset. Of the five individual runs, three had no detectable shifts. Only the last two had a 0.1% increase in gain. In the energy calibration, it was found best to employ the full and pair-escape energies of the well-known 2.6145-MeV line from Pb^{208*}, a

TABLE II. A summary of the Bi^{209} muonic x-ray energies as determined from Fig. 8 in comparison with CERN's (Ref. 5) results.

Peak channel in Fig. 8	Energy (keV)	Remarks on energy determination	CERN'S data[a]	Remarks
62.0 ±0.1	444.5±1.0	511 keV as reference	445.6±1.2	$5g \rightarrow 4f$
195.8 ±0.1	961.8±1.0	Use Pb^{208*} double-escape peak and full photopeak as calibrations	962.5±1.5	$4f_{7/2,5/2} \rightarrow 3d_{5/2}$
204.85±0.1	996.6±1.0		997.2±1.6	$4f_{5/2} \rightarrow 3d_{3/2}$
344.5 ±0.2	$(2552.8\pm1.0)-2mc^2$		$2554.8\pm2.0-2mc^2$	$(3d_{5/2} \rightarrow 2p_{3/2})-2mc^2$
360.6 ±0.1	$2614.47-2mc^2$		$2615.0-2mc^2$	$Pb^{208*}-2mc^2$
382.8 ±0.2	$(2699.5\pm1.0)-2mc^2$		$(2700.2\pm2.5)-2mc^2$	$(3d_{3/2} \rightarrow 2P_{1/2})-2mc^2$
611.5 ±0.4	(2553.2±1.6)		2554.8±2.0	$3d_{5/2} \rightarrow 2P_{3/2}$; full photopeak has much poorer statistics than pair-escape peak.
627.5 ±0.2	2614.47		2615±2	Pb^{208*}
650.0 ±0.4	2700.5±1.6		2700.2±2.5	$(3d_{3/2} \rightarrow 2P_{1/2})$ full photopeak has much poorer statistics than pair-escape peak.
1203.4 ±0.2	$(5841.5\pm3)-2mc^2$	Direct extrapolation from Pb^{208*} with nonlinearity uncertainty <0.05%	$(5839.7\pm5.5)-2mc^2$	$(2P_{1/2} \rightarrow 1S_{1/2})-2mc^2$
1253.2 ±0.3	$(6032.4\pm3)-2mc^2$		$(6032.2\pm5.0)-2mc^2$	$(2P_{3/2} \rightarrow 1S_{1/2})-2mc^2$

[a] Reference 5.

product of muon capture in Bi^{209} (Ref. 11):

$$Bi^{209}+\mu^- \rightarrow Pb^{208*}(3^-)+n+\nu_\mu$$
$$\searrow$$
$$Pb^{208}(0^+)+\gamma(2.61447\ \text{MeV}).$$

Since this nuclear γ line is detected and recorded simultaneously with the muonic x rays, its linewidth and line shape should serve as a standard monoenergetic γ line for comparison.

A summary of the Bi^{209} x ray energies is given in Table II. The K x ray energies were obtained by direct extrapolation from the Pb^{208*} nuclear γ rays. The uncertainty at the K x ray region was estimated by considering the integral nonlinearity of the system (<0.05%) over the 600-channel extrapolation involved. The energies below the 2.6145-MeV line were determined with the aid of the annihilation radiation line.

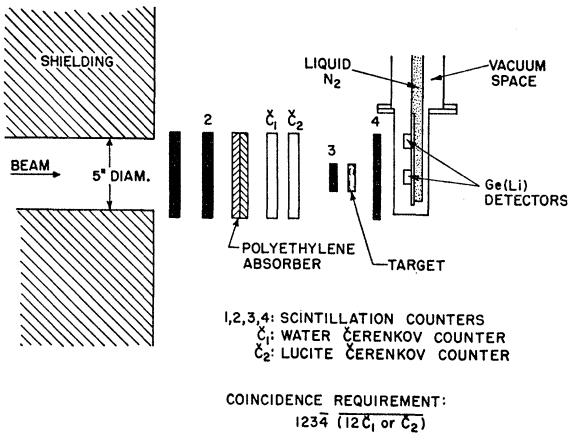

FIG. 4. The schematic drawing of the experimental arrangement of the beam telescope and the detectors.

2. *Intensities*

The counting rates of the x rays were determined directly from the total number of counts in the peaks after background subtraction. Owing to the inadequate statistics for both the peak and the background, the uncertainty estimated is $\sim\pm5\%$ for the K and L x rays and $\sim\pm1\%$ for the M x rays.

The counting-rate ratios are:

$$R_1=Y(2p_{3/2} \rightarrow 1s_{1/2}):Y(2p_{1/2} \rightarrow 1s_{1/2})=1.4\pm0.1,$$
$$R_2=Y(3d_{5/2} \rightarrow 2p_{3/2}):Y(3d_{3/2} \rightarrow 2p_{1/2})=1.46\pm0.1,$$

and

$$R_3=Y(4f_{7/2,5/2} \rightarrow 3d_{5/2}):Y(4f_{5/2} \rightarrow 3d_{3/2})=1.38\pm0.03.$$

To obtain the intensity ratios from the counting-rate ratios, we have applied the following corrections:

(i) The self-absorption in the Bi^{209} target which has an average surface density of 3 g/cm². A rough estimate shows that the total attenuations are $\sim7\%$ for K and L x rays and $\sim10\%$ for M x rays. The differences in attenuation within the K and L fine structures are $\simeq0.1\%$; those within the M x-ray fine structure are $\simeq0.4\%$.

(ii) The absorption in counter 4 of the beam telescope; the $\frac{1}{16}$-in. plastic scintillator attenuates K and L x rays by $<1\%$.

(iii) The absorption in the $\frac{1}{16}$-in.-thick aluminum container of the Ge(Li) detectors is negligible compared with the other losses.

(iv) Efficiency variation of the detector with energy; the efficiency (η) of the detector somewhat balances the above absorption effects. From a separate efficiency calibration of the detector, the relative change in detector efficiency $(\Delta\eta/\eta)_E$ over the energy range ΔE of

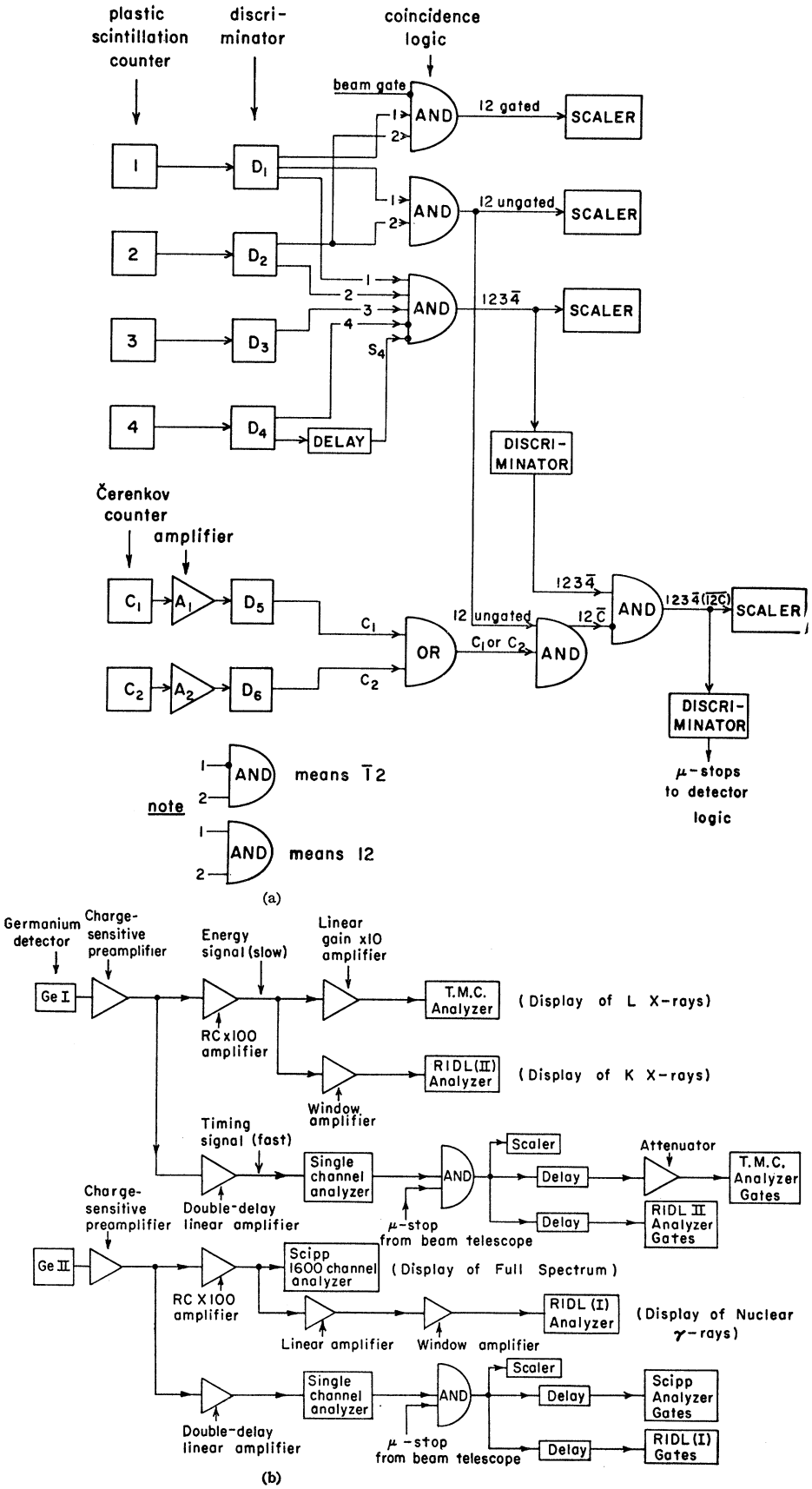

FIG. 5. (a) The logic diagram of the beam telescope to identify and count muons stopped in the target material. (b) The block diagram of the electronics related to the detectors to measure the x-ray energies and to provide the gating signals in coincidence with the stopping muons in the target.

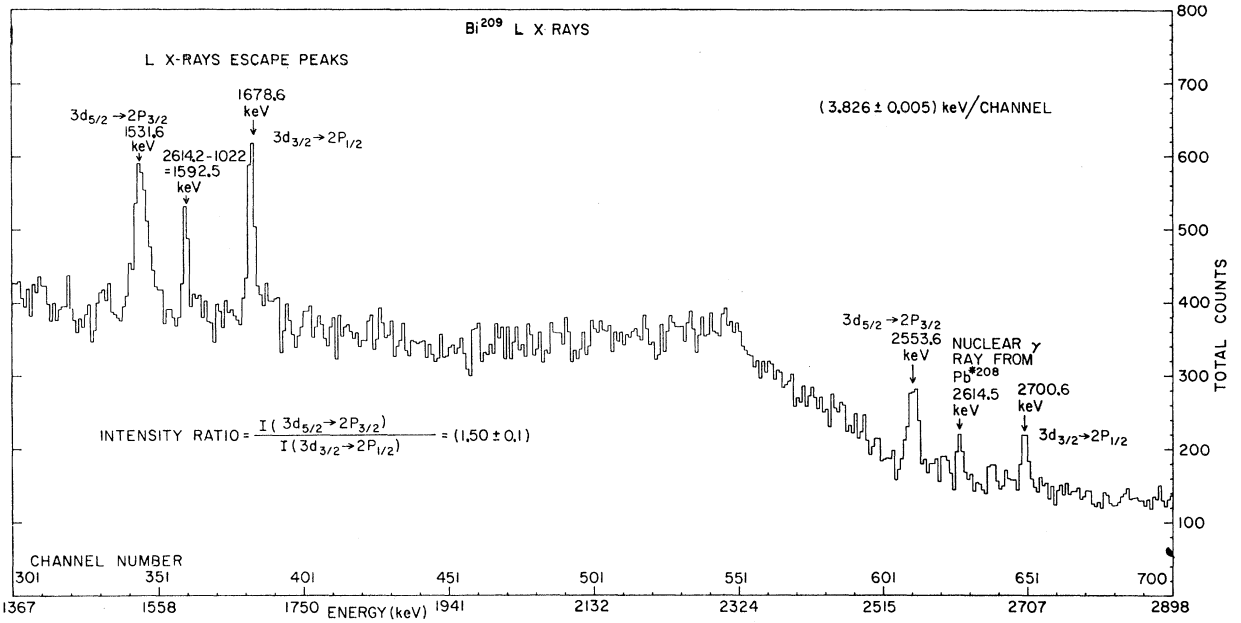

FIG. 6. The spectrum of the L x rays showing the full-energy as well as the double-escape peaks. The narrow line between the L x rays is a deexcitation γ ray from the reaction

$$Bi^{209}+\mu^- \rightarrow Pb^{208*}+n+\nu_\mu$$
$$\searrow Pb^{208*}+\gamma(2.6145\ \text{MeV}).$$

the fine structure is

$$\left(\frac{\Delta\eta}{\eta}\right)_{E=6\ \text{MeV},\ \Delta E=200\ \text{keV}} = 1.5\%$$

for the escape peaks of K x rays,

$$\left(\frac{\Delta\eta}{\eta}\right)_{E=2.7\ \text{MeV}\ \Delta E=150\ \text{keV}} \simeq 3\%$$

for the escape peaks of L x rays,

and

$$\left(\frac{\Delta\eta}{\eta}\right)_{E=1\ \text{MeV},\ \Delta E=35\ \text{keV}} \simeq -6\%$$

for M x rays.

Therefore, the corrected intensity ratios are:

$$I(2p_{3/2} \rightarrow 1s_{1/2}) : I(2p_{1/2} \rightarrow 1s_{1/2}) = 1.38 \pm 0.10$$
$$I(3d_{5/2} \rightarrow 2p_{3/2}) : I(3d_{3/2} \rightarrow 2p_{1/2}) = 1.50 \pm 0.10$$
$$I(4f_{7/2,5/2} \rightarrow 3d_{5/2}) : I(4f_{5/2} \rightarrow 3d_{3/2}) = 1.29 \pm 0.3$$

3. *hfs Broadening of X Rays*

Because of the unresolved hfs due to $M1$ or $M1$ and $E2$ interaction between the finite nucleus Bi^{209} and the muon, all the x rays appear as broadened lines if one compares either the $3d_{5/2} \rightarrow 2p_{3/2}$ or the $3d_{3/2} \rightarrow 2p_{1/2}$ transitions with the monoenergetic nuclear γ rays from Pb^{208*} (Fig. 6). For the K x rays there was no such convenient "built-in" monoenergetic γ ray recorded simultaneously on the spectrum for reference. A determination of the shape of a monoenergetic γ ray in the 6-MeV region was made by measuring the double escape peak of the 6.13-MeV γ rays from O^{16*} (3^-). A 1-min run of the O^{16*} spectrum showed a width $= (8.5 \pm 0.5)$ keV full width at half-maximum (FWHM) (Fig. 7). The broadening due to drifting and summing was estimated by comparing observed broadening of the 2.754-MeV γ ray from Na^{24} and the 2.6145-MeV γ ray from Pb^{208*}; it was concluded that a monoenergetic γ ray at the 5–6-MeV region would appear to have a FWHM (9.5 ± 0.5) keV on the summed spectrum. Natural linewidth is ~ 1 keV.[12]

In order to compare the experimental hyperfine structure with the theoretical prediction, both the $2p_{1/2} \rightarrow 1s_{1/2}$ and the $2p_{3/2} \rightarrow 1s_{1/2}$ transitions were fitted to the hfs theoretically calculated by Le Bellac.[7] Each hfs component was assumed to have a Lorentzian shape with a FWHM determined experimentally. The relative intensities of the components were calculated using statistical populations of the F levels, and the splitting was obtained as in Sec. II. The background was taken as a straight-line fit to the average background on both sides of the experimental broadened peak. The χ^2 test was applied to decide the best fit for each assumed nuclear model.

[12] W. B. Rolnick, Phys. Rev. **132**, 1110 (1963); J. Hufner, Institute for Theoretical Physics of Heidelberg University, Ph.D. thesis, 1965 (unpublished).

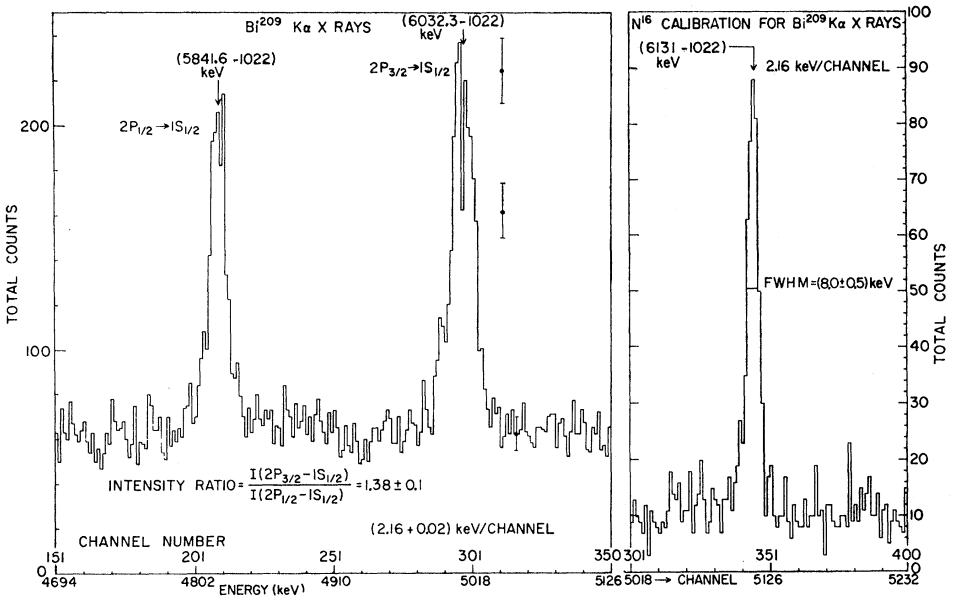

FIG. 7. The spectrum of the double-escape peaks of the K x rays, showing the broadening and splitting in the K x-ray doublet. To the right of the figure the 6.131-MeV γ ray from the N^{16} calibration is shown for line-shape comparison.

IV. DISCUSSION OF EXPERIMENTAL RESULTS AND CONCLUSION

The complete spectrum of the muonic x rays of bismuth is shown in Fig. 8, in which the double-escape peaks of the K x rays, the L x rays including both the full-energy photopeaks and the double-escape peaks, and the higher-order x rays are clearly seen. The $2s_{1/2} \rightarrow 2p_{1/2}$ transitions as calculated should occur between 1 and 2 MeV. However, no appearance of a line with a height above the statistical fluctuation of the background was found. From the experimental results, conclusions are obtained regarding the hfs of the K x rays, nuclear charge distribution, and intensity ratios.

A. hfs of the K x Rays

The lifetime of the p state is estimated to be $\sim 10^{-18}$ sec. Therefore, the natural linewidth should be ~ 1 keV.[12] In the $2p_{1/2} \rightarrow 1s_{1/2}$ transitions, only the $M1$ interaction between the nucleus and the muon occurs in the hfs. The χ^2 tests of the fitting of the experimental value to the various theoretical hfs for each of the assumed nuclear models (as listed in Table I) are shown in Table III.

As seen in Table III, the point-nucleus model gives the poorest fit to the experimental data. The best-fit model is obtained with a hfs constant which is 10% higher than the hfs constant for the configuration-mixing model. The test shows that the configuration-mixing model is more favorable than the single-particle model. Since there is only an 18% difference in the hyperfine energy splitting between these two models, better statistics and finer resolution of the K x-ray lines are highly desired; furthermore, drifts should be further reduced in the process of data taking in order to test how good the configuration model is. The construction of the resultant line from the constituent γ rays is shown in Fig. 9.

In the $2p_{3/2} \rightarrow 1s_{1/2}$ transitions, both the $M1$ and $E2$ interactions are present. For the $2p_{3/2}$ level, Le Bellac gave the values $A_1 = 0.83$ keV and $A_2 = -2.74$ keV. However, we have also tried values of A_2 which are 10, 20, and 40% larger than the value of -2.74 keV. A similar line-shape fitting to that used in the case of the $2p_{1/2} \rightarrow 1s_{1/2}$ transitions gave the results shown in Table IV. These results show that a wider separation of the constituent hyperfine lines fits the experimental data better, but even a 40% increase in A_2 does not bring the theoretical line shape within the experimental standard deviation as shown at the dip of Fig. 10. It is interesting to point out that a similar fitting by the Chicago group[13] also shows that a large value of A_2 fits their experimental curve better. Further refined

TABLE III. The results of the χ^2 test on the fitting for the $2p_{1/2} \rightarrow 1s_{1/2}$ transitions by using various nuclear models.

Model	Point nucleus	Single particle	Configuration mixing	Best fit $A_1(1+0.1)$
χ^2/channel[a]	1.547 A_1'	1.195 A_1^0	1.114 A_1	1.073
Centroid of the broadened peak	4821.7 keV	4821.7 keV	4822.8 keV	4822.8 keV
FWHM of each component	9.0 keV	9.5 keV	9.2 keV	9.0 keV

[a] χ^2/channel is defined [R. H. Moore, U. S. At. Energy Comm. NAS-NS 3107 (1962)] as

$$\frac{1}{N}\sum_{i=1}^{N}\left(\frac{(Y_i - Y_{pi})}{Y_i^{1/2}}\right)^2,$$

where $N = 38$ is the total number of channels fitted; Y_i is the actual number of counts in the ith channel, and Y_{pi} is the number of predicted or theoretical counts in the ith channel.

[13] The Chicago group used $A_2 = -4.0$ keV, which was computed with $Q = -0.466$ using a $\delta(r-R)$ form for the quadrupole charge distribution ρ_2. See S. Raboy *et al.*, Nucl. Phys. 73, 353 (1965).

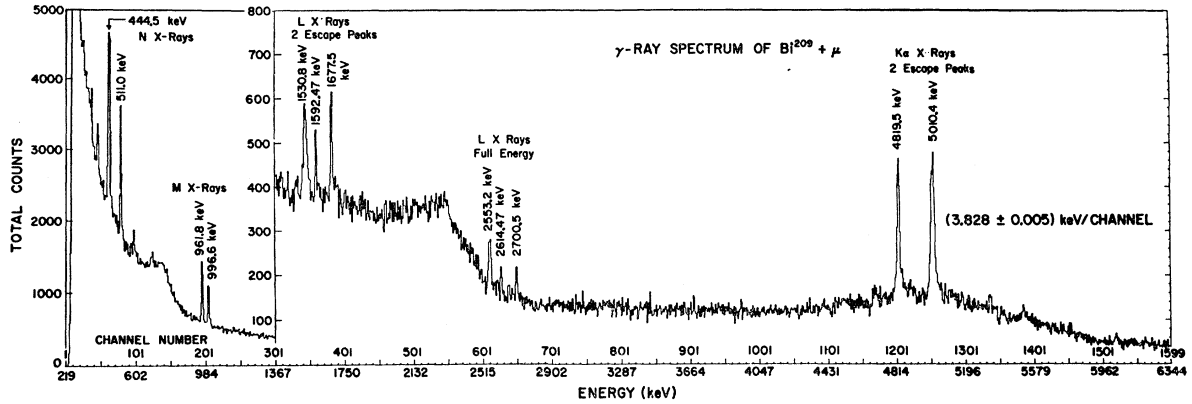

FIG. 8. The complete muonic x-ray spectrum of Bi^{209}, displayed on the SCIPP 1600. The energy region shown is from about 250 keV to 6.3 MeV.

results, both experimental and theoretical, are required to clarify this point. Probably, nuclear wave functions in a potential well of the Saxon-Woods type should be used instead of harmonic-oscillator wave functions such as Le Bellac used. On the other hand, since the $E2$ hyperfine splitting constant was calculated from the quadrupole moment deduced from the rather uncertain atomic electron-wave functions in the atomic-beam magnetic-resonance method and did not take into account the nuclear-volume effect, more sophisticated theoretical calculations are needed.

TABLE IV. The results of the χ^2 test on the fitting for the $2p_{3/2} \rightarrow 1s_{1/2}$ transitions by using various hfs constants.

Model	Point nucleus	Single particle	Configuration mixing	Best fit
A_2(keV), hfs constant for $E2$ interaction	−2.74	−3.01	−3.29	−3.83
χ^2/channel	1.47	1.30	1.19	1.17
Centroid of broadened peak (keV)	5011.7	5012.7	5012.7	5012.7
FWHM of each component (keV)	10.2	9.1	9.1	9.1

B. Nuclear Charge Distribution

From the muonic x-ray transition energies information on the nuclear charge distribution can be obtained. The muon binding energies for all states are obtained by solving the Dirac equation, in which the electrostatic potential[8] of an assumed nuclear charge distribution, with the vacuum polarization potential included, is used. Therefore, the calculated binding energies depend on the nuclear model assumed. For a spherical nucleus, the Fermi distribution seems to yield results closest to some previous experimental data.[14] The Fermi charge distribution has the form:

$$\rho=\rho_0 \Big/ \left\{1+\exp\left[(4\log_e 3)\left(\frac{r-c}{t}\right)\right]\right\},$$

TABLE V. The theoretical values of each transition energy obtained from the best-fit c, t values of the nuclear charge Fermi distribution.

Transition	Experiment	Theory
$2p_{1/2} \rightarrow 1s$	5841.5±3	5841.87
$2p_{3/2} \rightarrow 1s$	6032.4±3	6032.03
$3d_{3/2} \rightarrow 2p_{1/2}$	2699.5±1	2699.52
$3d_{5/2} \rightarrow 2p_{3/2}$	2552.8±1	2554.18
$4f \rightarrow 3d_{3/2}$	996.6±1	996.68
$4f \rightarrow 3d_{5/2}$	961.8±1	961.06
$5g \rightarrow 4f$	444.5±1	444.93

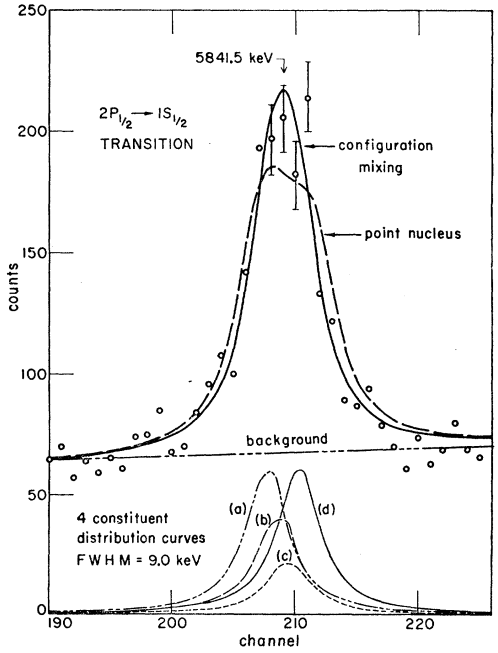

FIG. 9. The comparison of the experimental and the calculated values of the hfs of the $2p_{1/2} \rightarrow 1s_{1/2}$ transition. The four constituent lines shown are calculated by using the configuration-mixing model.

[14] G. E. Pustovalov, Zh. Eksperim. i Teor. Fiz. **43**, 2170 (1962) [English transl.: Soviet Phys.—JETP, **16**, 1534 (1963)].

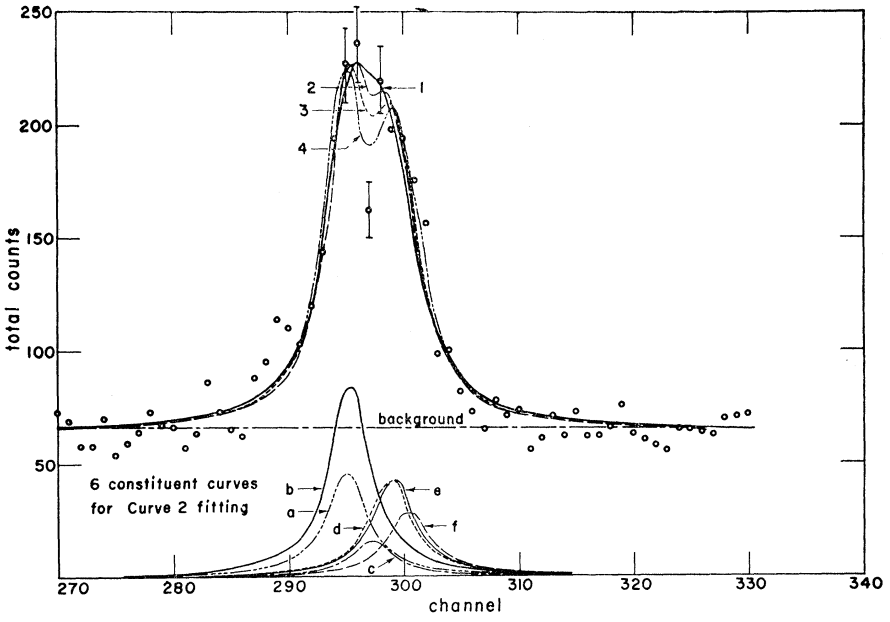

2.16 keV/channel

Number of parameters in fitting = 5

Total channels for fitting = 60 channels

χ^2/channel expected = 1.09

Comparison with the Resultant Theoretical Curves

curve	A_2 (keV)	χ^2/chan.	centroid	line width
1	-2.74	1.47	297.0	10.2 keV
2	-3.01	1.30	297.1	9.1 keV
3	-3.29	1.19	297.1	9.1 keV
4	-3.83	1.17	297.1	9.1 keV

Energy Shift in keV of Centroid from Unperturbed Transition

curve	A_2 = -2.74	A_2 = -3.01	A_2 = -3.29
a	-4.04	-4.51	-5.04
b	-3.54	-3.81	-4.08
c	-0.13	0.37	0.58
d	3.03	3.49	3.94
e	3.76	4.00	4.21
f	6.66	7.12	7.57

Intensities of individual curves are based on statistical population of the states.

FIG. 10. The experimental observation of the hfs for the $2p_{3/2} \rightarrow 1s_{1/2}$ transition and comparison with the theoretical values. The curves for the six constituent lines are drawn using the experimental line shapes for monochromatic nuclear γ rays, with theoretical intensities and spacings calculated as in Fig. 2 but for $A_2 = -3.01$ keV. The resultant curves have various A_2 values: curve 1, $A_2 = -2.74$ keV; curve 2, $A_2 = -3.01$ keV (10% increase); curve 3, $A_2 = -3.3$ keV (20% increase); curve 4, $A_2 = -3.8$ keV (40% increase). Curve 4 shows the closest fit to the experimental values.

where c and t are the two parameters of the distribution; c is the radius where the distribution falls to $\frac{1}{2}$ of ρ_0 and t is the skin thickness in which the distribution falls from 90 to 10% of ρ_0.

The relationship between c and t for any given transition energy can be represented by an isoenergetic curve in the c-t plane.[15] The experimental data give the following transition energies:

(1) $E(2p_{1/2} \rightarrow 1s_{1/2})$, (2) $E(2p_{3/2} \rightarrow 1s_{1/2})$,
(3) $E(3d_{3/2} \rightarrow 2p_{1/2})$, (4) $E(3d_{5/2} \rightarrow 2p_{3/2})$,
(5) $E(4f_{5/2} \rightarrow 3d_{3/2})$, (6) $E(4f_{7/2} \rightarrow 3d_{5/2})$,
(7) $E(5g \rightarrow 4f)$.

Each isoenergetic curve will give a relation between c and t on the c-t plane; if experimental uncertainties are included, the curve smears out to a band. Since each transition responds differently to changes in c and t, a realistic model should give a set of c and t values which provide consistent results for all observed transition energies. On the c-t diagram, the experimental transition energies are used to calculate the c-t curves in Fig. 11.

[15] R. C. Barrett (private communication).

In order to obtain a quantitative estimate of the errors in c and t, a least-squares fit to the seven energies was carried out. The errors in c and t were not obtained from the error matrix, but rather from a set of calculations of χ^2 made for different fixed values of t in which c was allowed to vary as a free parameter. The values of c and t obtained were:

$$c = (1.126_{-0.006}^{+0.008})A^{1/3}\,\text{fm} = 6.682_{-0.036}^{+0.047}\,\text{fm},$$
$$t = (0.511_{-0.033}^{+0.026})(4\log_e 3)\text{fm} = 2.248_{-0.145}^{+0.114}\,\text{fm}.$$

The c and t values are strongly correlated as seen in Fig. 11. The errors are taken as the 70% confidence limits from the χ^2 test. This corresponds to an equivalent rms radius $R = 7.118 \pm 0.086$ fm, where R is defined by

$$R = \sqrt{(5/3)}\langle r^2\rangle_{\text{av}}^{1/2}.$$

Other determinations of c and t for Bi^{209} may be found in the work of Acker *et al.*[5] and Anderson *et al.*[16]

[16] H. L. Anderson, C. K. Hargrove, E. P. Hincks, and A. J. Tavendale, in *Proceedings of the 12th Annual International Conference on High-Energy Physics, Dubna, 1964* (Atomizdat, Moscow, 1965); H. L. Anderson, R. J. McKee, C. K. Hargrove, and E. P. Hincks, in Proceedings of Williamsburg Conference on Intermediate Energy Physics, 1966 (unpublished).

TABLE VI. Bi^{209} intensity ratios for K x-ray, L x-ray, and M x-ray fine structures.

Experimental group	$\frac{I(2p_{3/2} \rightarrow 1s_{1/2})}{I(2p_{1/2} \rightarrow 1s_{1/2})}$	$\frac{I(3d_{3/2,5/2} \rightarrow 2p_{3/2})}{I(3d_{3/2} \rightarrow 2p_{1/2})}$	$\frac{I(3d_{5/2} \rightarrow 2p_{3/2})}{I(3d_{3/2} \rightarrow 2p_{1/2})}$	$\frac{I(4f \rightarrow 3d_{5/2})}{I(4f \rightarrow 3d_{3/2})}$
Frati *et al.*[a]	1.34 ±0.08	1.70±0.06		
Acker *et al.*[b]	1.2 ±0.3	1.35±0.5		
Anderson *et al.*[c]	1.23 ±0.18	<1.92		
Ehrlich *et al.*[d]	1.43 ±0.06		1.43±0.07	
CERN[d]	1.31 ±0.20	1.44±0.20		1.18±0.12
Our result	1.38 ±0.10		1.50±0.10	1.29±0.3
Theoretical	1.920	1.92	1.75	1.49

[a] Reference 2.
[b] H. L. Acker, G. Backenstoss, C. Daum, J. C. Sens, and S. A. DeWit, Phys. Letters **14**, 317 (1965).
[c] Reference 16.
[d] Reference 5.

Table V shows the theoretical values of each transition energy calculated for the charge distribution which gave the best fit.

In comparison, the electron scattering data[17] give:

$$c=(1.13\pm0.013)A^{1/3}\text{ fm}=6.73\pm0.08\text{ fm},$$
$$t=(0.482\pm0.036)(4\log_e 3)\text{fm}=2.12\pm0.16\text{ fm}.$$

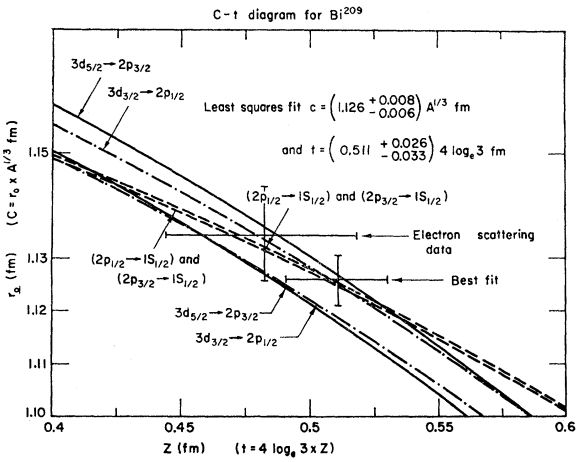

FIG. 11. The c-t diagram of the nuclear charge distribution

$$\rho=\rho_0\left\{1+\exp\left(\frac{r-c}{t}\right)4\log_e 3\right\}^{-1}.$$

The curves shown are the iso-energetic plots for the observed transition energies. The two K x rays—the $2p_{1/2} \rightarrow 2s_{1/2}$ and the $2p_{3/2} \rightarrow 1s_{1/2}$ transitions—almost overlap each other. The observed energy uncertainties in the L x rays are included; in the $3d_{3/2} \rightarrow 2p_{1/2}$ and the $3d_{5/2} \rightarrow 2p_{342}$ transitions each covers a band in the c-t plane. The M x rays are relatively insensitive to the c-t values. The least-squares fit shows that

$$c=(1.126_{-0.006}{}^{+0.008})A^{1/3}\text{ fm}=6.682_{-0.036}{}^{+0.047}\text{ fm},$$
$$t=(0.511_{-0.033}{}^{+0.026})(4\log_e 3)\text{ fm}=2.248_{-0.145}{}^{+0.114}\text{fm}.$$

This may be compared with the electron scattering data:

$$c=(1.13\pm0.013)A^{1/3}\text{ fm}=6.73\pm0.08\text{ fm},$$
$$t=(0.482\pm0.036)(4\log_e 3)\text{ fm}=2.12\pm0.16\text{ fm}.$$

[17] G. J. C. von Niftrik and R. Engfer, Phys. Letters **22**, 490 (1966).

The uncertainties in the nuclear parameters determined by muonic x rays are several times smaller. However, the results between these two methods are in good agreement within the uncertainties specified. With further improvement in the statistics and stability of muonic measurements, one should be able to determine the value of c to an accuracy of 0.1% and t to 1%.

C. Intensity Ratios

The observed intensity ratios for the K, L, and M fine structures are (1.38±0.10), (1.50±0.10), and (1.29±0.3), respectively. The theoretical intensity calculation assuming that all muonic states are populated according to the statistical weight gives the corresponding intensity ratios 2, 1.8, and 1.5. If the energy dependence within the fine structure is not neglected compared with the transition energy, then the theoretical intensity ratios are 1.92, 1.75, and 1.49. There have been several theoretical attempts[12] to explain the intensity anomaly, but so far, none has been supported by the experimental evidence. Table VI summarizes the experimental values on the intensity ratios.

ACKNOWLEDGMENTS

The authors wish to express their profound appreciation to W. Patton and Professor L. J. Lidofsky for their most valuable help on our data analysis on the PDP-4 computer. The electronics used in the experiment were designed and built by our electronic group under the guidance of J. Hahn, V. Guiragossian, and T. Becker. We particularly wish to take this opportunity to thank W. L. Hansen of the University of California and Dr. F. P. Ziemba of the Solid State Radiation Counter Laboratory for their valuable counsel on the fabrication of the Ge detectors. We are indebted to William Hunt and the cyclotron crew for their efforts in operating the accelerator.